Energy 224 (2021) 120142

Contents lists available at ScienceDirect

Energy

journal homepage: www.elsevier.com/locate/energy

Carbon-coated oxygen vacancies-rich Co_3O_4 nanoarrays grow on nickel foam as efficient bifunctional electrocatalysts for rechargeable zinc-air batteries

Dongfang Chen [a, b], Lyuming Pan [a, b, c, **], Pucheng Pei [a, b, *], Shangwei Huang [a, b], Peng Ren [a, b], Xin Song [a, b]

[a] State Key Lab. of Automotive Safety and Energy, Tsinghua University, Beijing, 100084, China
[b] School of Vehicle and Mobility, Tsinghua University, Beijing, 100084, China
[c] Tsinghua Shenzhen International Graduate School, Tsinghua University, Shenzhen, 518055, China

ARTICLE INFO

Article history:
Received 26 December 2020
Received in revised form
16 February 2021
Accepted 17 February 2021
Available online 23 February 2021

Keywords:
Rechargeable zinc-air batteries
Bifunctional electrocatalysts
Oxygen vacancies-rich
Carbon-coated
Oxygen reduction reaction

ABSTRACT

The bifunctional electrocatalyst has an important influence on the power output and cycle life of rechargeable zinc-air batteries. Cobalt oxides, especially Co_3O_4, have attracted much attention due to their high catalytic activity for oxygen evolution reaction (OER). It is difficult to improve the catalytic activity of oxygen reduction reaction (ORR) for rechargeable zinc-air batteries. In this paper, Co_3O_4 containing rich oxygen vacancies is prepared by in-situ growth on the nickel foam, and the carbon coating treatment on the surface increases the conductivity and stability of Co_3O_4, which prolongs its cycle life. The results show that moderate oxygen vacancies can achieve the best catalytic performance. The peak power density of zinc-air battery assembled by this air electrode can reach 54.5 mW cm^{-2}, which is 51.4% higher than that of the untreated Co_3O_4 catalyst. The cycle life of the battery can reach 716 cycles (358 h), prolonging about 250 h compared with Co_3O_4 without carbon coating treatment. It is proved that the improved Co_3O_4 can increase the power output and cycle life of the rechargeable zinc-air battery, which helps to expand the application range of cheap Co_3O_4 catalyst, and provides an effective and economic solution to obtain excellent electrocatalysts for metal-air batteries.

1. Introduction

With the rapid development of industry, energy consumption is increasing. Coal, oil, natural gas, and other fossil energy still occupy the mainstream of energy consumption [1]. However, the reserves of fossil energy are limited, and it is difficult to maintain the high-speed growth of consumption demand for a long time. In addition, the exhaust emissions of using fossil energy have a harmful impact on the environment and human body containing with toxic and harmful gases, greenhouse gases and micro nano particles [2]. With the increase of fossil energy consumption and the increasing serious environmental pollution problems, cheaper and environmentally friendly energy storage and conversion technologies, are paid more and more attention, such as lithium-ion batteries [3–5], fuel cells [6–8], solar cells [9,10], supercapacitors [11,12], metal-air batteries [13,14], and so on.

The theoretical specific energy of zinc-air battery is 1350 Wh·kg^{-1}, while the theoretical specific energy of lithium-ion battery is 265 Wh·kg^{-1} [15]. Therefore, zinc-air batteries have the potential to solve the problem of insufficient specific energy of lithium ion battery. The resources of zinc are rich and the mining and refining industry of zinc is relatively mature, which have more advantages than the expensive lithium metal [16]. Moreover, the anode, cathode and electrolyte of zinc-air batteries are stored separately and modularized to facilitate long-term storage. Zinc-air batteries have become a potential energy storage technology due to its high theoretical specific energy, simple structure, safety and environmental protection [17–19]. At present, the main problems of zinc-air batteries are low actual power density and short cycle life [20,21], which are closely related to the bifunctional electrocatalysts of rechargeable zinc-air batteries. Although the actual

* Corresponding author. State Key Lab. of Automotive Safety and Energy, Tsinghua University, Beijing, 100084, China
** Corresponding author. State Key Lab. of Automotive Safety and Energy, Tsinghua University, Beijing, 100084, China.
E-mail addresses: plm14@tsinghua.org.cn (L. Pan), pchpei@mail.tsinghua.edu.cn (P. Pei).

https://doi.org/10.1016/j.energy.2021.120142
0360-5442/

power density of zinc-air battery is higher than that of vanadium-air flow battery and lithium-air battery, the current progress is difficult to meet the needs of industrialization [22]. The imbalance of hydrophilicity and hydrophobicity of air cathode, the generation of by-products and bubble growth of zinc anode, the evaporation and decomposition of electrolyte and other problems will result in lower actual power density of zinc-air battery [23]. But most importantly, the low catalytic activity and instability of oxygen catalyst are the main reasons for the low actual power density of zinc-air batteries, which hinder its commercialization and practical application.

Oxygen is always involved in the reaction on the air electrode in zinc-air batteries. During the discharge process, ORR occurs at the air electrode, and OER occurs during the charging process [24,25]. For the electrocatalysts, zinc-air primary battery and zinc-air mechanically rechargeable battery only require a good ORR catalytic activity, while the rechargeable zinc-air battery requires both OER and ORR bifunctional catalytic activity. Pt/C, a commonly used noble metal catalyst, has a high catalytic activity for ORR [26–28], but its reaction power for catalytic OER is poor. Generally speaking, the OER activity of noble metal oxides (RuO_2 and IrO_2) is better [29,30]. Although the noble metal catalyst has high catalytic activity, the cycle stability is not ideal and the price is quite expensive, which makes it difficult to reduce the cost of zinc-air batteries [31]. Researchers believe that transition metal based electrocatalysts are expected to replace noble metal catalysts. Among them, various manganese based catalysts (α-MnO_2 [32], β-MnO_2 [33], MnOOH [34]) can show excellent ORR catalytic activity, but they are not enough to meet the requirements of rechargeable zinc-air batteries due to its relatively poor OER activity and charge-discharge cycle stability [35,36].

Cobalt based electrocatalyst has become a research hotspot because of its strong OER catalytic activity. More and more researches have tried to apply cobalt based electrocatalyst to zinc-air batteries [37–39]. Co_3O_4 is widely concerned which is a kind of cobalt oxides. The main focus is to improve its electrocatalytic activity for ORR [40,41]. There are three methods reported in the literature: increasing the specific surface area of Co_3O_4, compounding it with materials with high oxygen reduction activity and enhancing the intrinsic catalytic activity of Co_3O_4. Park et al. [42] prepared 3D honeycomb mesoporous cobalt oxide (3DOM Co_3O_4) by template methods. Because of its porous and strong structure, 3DOM Co_3O_4 is superior to Co_3O_4 bulk and greatly enlarges the surface area of the catalyst, thus increasing the number of active centers. The larger exposure area usually provides more active sites for ORR and OER to improve the electrocatalytic performance. Due to the limited ORR catalytic activity of Co_3O_4, the scheme of increasing reaction interface through porous structure has a limitation on the performance improvement. Hence, it is a simple solution to combine Co_3O_4 with doped carbon materials [43], manganese oxides [44] and other high efficiency ORR catalysts. Guan et al. [45] embedded the irregular hollow Co_3O_4 nanospheres into the N-doped carbon nanowall array (NC—Co_3O_4). Owing to the change of the electronic structure caused by the doping atoms in the carbon materials and the synergistic effect produced by the combination with Co_3O_4, an open circuit potential of 1.44 V and a capacity of 387.2 mAh·g^{-1} (based on the total mass of zinc and catalyst) for zinc-air batteries were achieved. However, such composite materials are usually in powder form and need to be connected to the collector by adhesive. In the process of multiple charge and discharge cycles, the continuous corrosion and erosion of the electrolyte on the adhesive can cause the catalyst to fall off gradually, which will adversely affect the durability of rechargeable zinc-air batteries [46].

Recently, the new idea to enhance the intrinsic oxygen reduction catalytic activity of Co_3O_4 nanomaterials based on in-situ growth in the collector. Yu et al. [47] prepared nitrogen doped Co_3O_4 nanowires by heat treatment in NH_3 atmosphere. Compared with the original Co_3O_4 electrode, all N-doped Co_3O_4 electrodes increased the ORR onset potential from 0.83 V to 0.94 V, which confirmed that the introduction of nitrogen into Co_3O_4 can significantly improve the catalytic activity. Ma et al. [48] obtained Co_3O_4 nanowires rich in oxygen vacancies by argon plasma treatment. Due to the regulation of oxygen vacancy on Co^{2+} and Co^{3+} valence state, the oxygen reduction peak potential increased from 0.69 V to 0.81 V, and the slope of Tafel curve decreased from 220 mV·dec^{-1} to 58 mV·dec^{-1}, which proved that oxygen vacancy could enhance the intrinsic catalytic activity of Co_3O_4. However, the energy consumption from low valence Co to active intermediate is higher than that from high valence Co [49]. Excessive plasma treatment increases the oxygen vacancy and low valence Co, and increases the required energy consumption, which leads to the reduction of reaction kinetics. Therefore, it is necessary to further study the effect of oxygen vacancy on the ORR catalytic performance of Co_3O_4. In addition, the long-term cycling stability of rechargeable zinc-air batteries is also challenged by directly exposing oxygen vacancies-rich materials to the alkaline electrolyte.

In this paper, carbon-coated oxygen vacancies-rich Co_3O_4 as efficient bifunctional electrocatalysts for rechargeable zinc-air batteries. Co_3O_4 treated by Ar plasma has a lot of oxygen vacancies, showing a higher catalytic activity for oxygen reduction than untreated Co_3O_4. The onset potential and Tafel slope of the optimized carbon-coated oxygen vacancies-rich Co_3O_4 electrode are 0.963 V and 129 mV·dec^{-1}, and the Tafel slope is much lower than those of carbon-coated Co_3O_4 (271 mV·dec^{-1}) and Co_3O_4 under other treatment conditions. The peak power density of zinc-air batteries assembled with the new catalyst increased from 36.0 mW cm^{-2} to 54.5 mW cm^{-2}. Because the new catalyst was directly grown on the collector and the carbon coating protected the oxygen vacancies, the zinc-air battery showed an ultra-long charge and discharge cycle life of 358 h.

2. Experimental

2.1. Preparation of Co_3O_4/Ni Foam

Co_3O_4/Ni Foam was prepared by hydrothermal method as previously reported [50]. A typical synthesized procedure is shown in Fig. 1a. Firstly, the cobalt precursor array was prepared. Cut the nickel foam with a size of Φ 19.5, dip in 3.0 mol L^{-1} HCl solution, ultrasonic treatment 10 min to remove the surface oxide layer, then take it out and wash it with deionized water for three times, dry and reserve. 2 mmol $Co(NO_3)_2·6H_2O$, 8 mmol NH_4F, 10 mmol $CO(NH_2)_2$ were weighed and dissolved in 40 mL deionized water for standby. The pretreated nickel foam was placed in the bottom of the inner cavity of the PTFE liner of a 50 mL high pressure water reaction kettle and poured into the preconfigured solution. The reactor was tightened and placed in a constant temperature box (Shanghai Yiheng Scientific Instrument Co., Ltd., DZF-6051), kept at 120 °C for 6 h, and then cooled naturally to room temperature. The obtained products were washed by deionized water for several times and then dried naturally. The product was cobalt precursor nano array grown on nickel foam (labeled Co(OH)F/Ni Foam). The Co(OH)F/Ni Foam was placed in a high-temperature chamber furnace (Shanghai Sager Furnace Co., Ltd., SG-QF) and heated to 350 °C at 5 °C·min^{-1} heating rate in air and maintained at 2 h. The product of Co_3O_4 nano array was grown on foam nickel (labeled Co_3O_4/Ni Foam) after the natural cooling of the furnace. The loading capacity of Co_3O_4 is about 0.2 mg cm^{-2}. All chemical reagents are of

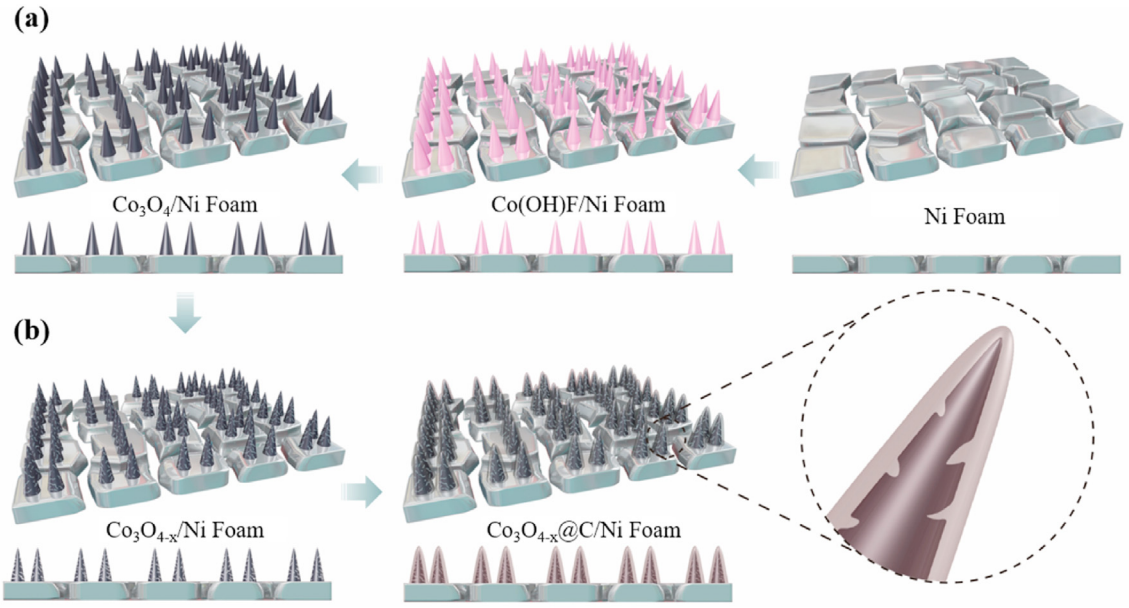

Fig. 1. Schematic illustration of synthesized procedure of (a) Co_3O_4/Ni Foam and (b) Co_3O_{4-x}@C/Ni Foam.

analytical purity.

2.2. Preparation of Co_3O_{4-x}@C/Ni Foam

A typical synthesized procedure is shown in Fig. 1b. The Co_3O_4/Ni Foam is placed in the plasma photolithography chamber (DRY-TEK LLC. MS-5). Under the atmosphere of 320 SCCM argon and 20 SCCM oxygen, the plasma is processed at 1 min, 3 min and 5 min respectively under 500 W power. After the treatment is finished, the product is Co_3O_4 nanoarrays enriched with oxygen vacancies naturally grown on nickel foam, labeled as Co_3O_{4-x}/Ni Foam (1 min), Co_3O_{4-x}/Ni Foam (3 min), Co_3O_{4-x}/Ni Foam (5 min), respectively。

The sample was immersed in a 0.04 mol L^{-1} glucose solution for 24 h then took out and placed in a high temperature chamber furnace (Shanghai Sager Furnace Co., Ltd., SG-QF). The temperature was heated to 450 °C at the heating rate of 5 °C·min^{-1} in argon atmosphere and maintained at 2 h. After the natural cooling of the furnace, the carbon-coated oxygen vacancies-rich Co_3O_4 nanoarray was grown on nickel foam, labeled as Co_3O_{4-x}@C/Ni Foam (1 min), Co_3O_{4-x}@C/Ni Foam (3 min), Co_3O_{4-x}@C/Ni Foam (5 min), respectively.

2.3. Preparation of air electrodes

According to the method as previously reported [51], Co_3O_4/Ni Foam or Co_3O_{4-x}@C/Ni Foam sheet was treated by hydrophobic treatment. In brief, the sheet is completely immersed in PTFE emulsion (5 wt%, Shanghai Hesen Electric Co., Ltd) for 1 min and then placed in the air at 60 °C for 20 min. After soaking and drying, the sheet should be placed in air atmosphere, heated to 300 °C for 1 h at a heating rate of 5 °C·min^{-1}, and then cooled naturally with the furnace for standby. The content of PTFE was 0.2 mg cm^{-2}. The treated Co_3O_4/Ni Foam or Co_3O_{4-x}@C/Ni Foam sheet was overlapped with commercial hydrophobic diffusion layer, and air electrode was obtained by hot pressing (Shenzhen Xotech Technology Co., Ltd., TH-XC605-HC200) three times under certain conditions (hot pressing surface temperature 80 °C, hot pressing pressure 0.5 MPa). The thickness of air electrode is 0.3 mm.

2.4. Materials characterization

The composition analysis of the composite was carried out in an X-ray diffractometer (Bruker, D8) operating at 40 keV using a Cu-Kα source. The microstructure was observed by scanning electron microscope (SEM, Carl Zeiss AG Merlin) at 5 kV. Energy dispersive X-ray spectroscopy (EDS) was used to analyze the types and contents in the micro region of the materials at an accelerating voltage of 15 kV. The geometrical properties of the materials were measured by X-ray photoelectron spectroscopy (XPS) data at 350 W using physical electronic PHI 5600 multi technology system. The hydrophobicity of different electrode surfaces was characterized by contact angle measurement system (DataPhysics, OCA25). The EPR spectra were obtained using a CIQTEK EPR-100 spectrometer at 120 K.

2.5. Electrochemical performance test

5 mg catalyst, 1 mL ethanol and 10 μL Nafion solution (5 wt%) were mixed, and the mixture was ultrasonic treated for 30 min 8 μL mixed liquid was absorbed with a micropipette and dropped in the area of Φ 5 mm in the center of the disc electrode, so that the droplets evenly covered the glassy carbon on the electrode surface. When the catalyst was slowly dried at room temperature for 24 h, the catalyst on the surface of glassy carbon was uniformly loaded without any abnormal phenomena such as coffee ring and falling off. At this time, the catalyst loading was 0.2 mg cm^{-2}, which could be used for further experiments.

According to the method reported in the literature [52], the OER and ORR properties of the catalyst were measured by typical three electrode system on the electrochemical workstation (Princeton Applied Research, VersaSTAT 3F). The electrolyte of electrode system is 0.1 mol L^{-1} KOH solution. Ag/AgCl electrode fill with 10% KNO_3 and Pt wire were used as reference electrode and counter electrode respectively. The catalyst coated on glass carbon electrode (5 mm in diameter) was selected as the working electrode.

Firstly, KOH solution saturated with nitrogen was used as electrolyte to activate the catalyst on the electrode surface. In the typical scheme, cyclic voltammetry (CV) scanning is carried out

continuously for 15 cycles between −0.147 V−1.197 V (vs. RHE), which makes the CV curves of the last three cycles obviously coincide. Five CV tests were carried out between 1.097 V−1.797 V (vs. RHE) and −0.147 V−1.197 V (vs. RHE). The last set of data was used as the background current of OER and ORR. During the whole process, nitrogen continuously flows into the reaction tank to keep the nitrogen saturated.

Next, the electrolyte was replaced with an oxygen saturated KOH solution. Electrochemical impedance spectroscopy (EIS) was used to measure the working electrode in the low anodic polarization overpotential region. The frequency range and amplitude of EIS are 0.01−100 000 Hz and 5.0 mV, respectively. Five groups of CV curves were obtained at different scanning rates (50 mV s^{-1}, 100 mV s^{-1}, 150 mV s^{-1}, 200 mV s^{-1}, 250 mV s^{-1}) in the voltage range of 0.927 V−1.017 V (vs. RHE). The electrochemical active surface area (ECSA) was determined by the dependence of current and scanning rate in the CV curve. According to the same method, the volt ampere characteristics of OER and ORR were recorded, and the LSV curve was obtained by averaging the CV curve data. The OER results were corrected by 90% iR at 10 mV s^{-1}. Five groups of ORR curves were obtained at different glassy carbon electrode rotate speeds (2500 rpm, 1600 rpm, 900 rpm, 625 rpm and 400 rpm). The electron transfer number was determined by the dependence of current and electrode rotate speed in the curves. In the whole experiment, oxygen saturation was maintained by continuously injecting oxygen into the electrolyte.

Finally, all potentials in operation were converted into potential versus reversible hydrogen electrode (RHE): $E_{RHE} = E_{Ag/AgCl} + 0.199 + 0.0591 \times pH$. The electron transfer number of oxygen molecule in ORR process is calculated. The Tafel slopes of OER and ORR are calculated according to the low overpotential cross section of LSV curves.

2.6. Assembly and test of zinc-air batteries

The prepared air electrode was used as positive electrode, zinc foil (0.2 mm) after acid treatment was used as negative electrode, and 6 mol L^{-1} KOH + 0.02 mol L^{-1} ZnO solution was used as electrolyte. The geometric area of positive electrode exposed to air is about 1 cm^2, which is the same as that of zinc foil and catalyst layer exposed to the electrolyte. The measurement was carried out in ambient air using the same electrochemical workstation (VersaSTAT 3F, Princeton Applied Research) as the three electrode system. The Galvano dynamic discharge voltage profiles of the battery were measured at a voltage step of 10 mV s^{-1} from open circuit voltage to 0.4 V. The cycling stability was tested at 10 mA cm^{-2} with a fixed time interval (15 min for discharge followed by 15 min for charge).

3. Results and discussion

3.1. Morphology, crystal structure and chemical composition

The morphology of Co_3O_4, Co_3O_{4-x} and Co_3O_{4-x}@C were observed by scanning electron microscopy. The Co_3O_4 nanoarrays are uniformly distributed on the nickel foam substrate and consist of dense arranged nanowires. The length of each nanowire is more than 1 μm and the width is about 20−100 nm, as shown in Fig. 2a. It is worth noting that the surface of Co_3O_4 nanowires is smooth, which shows the integrity of the material growth in hydrothermal reaction. After argon plasma treatment, the shape and size of the nanowires did not change, but obvious irregular spots and pits can be observed on the surface (Fig. 2b). This is caused by the oxygen vacancy on the surface of Co_3O_{4-x} due to the impact damage of argon plasma. After soaking in glucose solution and calcining, the surface of nanowires is covered with a rough carbon film, and the thickness of nanowires increased significantly (Fig. 2c). In order to further confirm the formation of Co_3O_4, XRD was used to analyze the crystal structure of the Co_3O_4 before and after growing on the nickel foam. Nickel foam shows only two peaks representing nickel, indicating that the collector cleaned by hydrochloric acid and deionized water is not obviously oxidized and doesn't contain a large number of other impurities. As shown in Fig. 2d, at 22.1°, 36.3°, 42.8°, 65.3° and 69.7° correspond to (111), (220), (311), (511) and (440) of Co_3O_4 (JCPDS 42−1467). It is noteworthy that the reflection peak of nickel at 52.0° and 60.9° has a similar height to the characteristic peak of Co_3O_4, indicating that Co_3O_4 nanowires are well covered on the nickel foam substrate. At the same time, EDS results (Fig. 2e) show uniform distribution of Ni, Co and O, which clearly shows that Co_3O_4 nanoarrays adhere uniformly to the

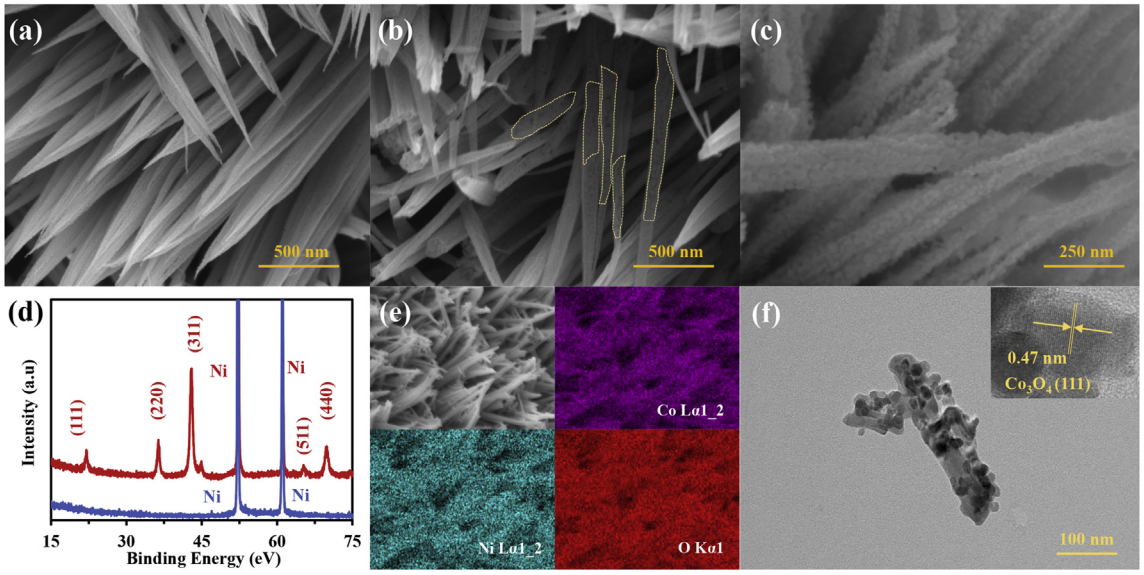

Fig. 2. SEM images of (a) Co_3O_4, (b) Co_3O_{4-x} and (c) Co_3O_{4-x}@C. (d) X-ray diffraction images of nickel foam and Co_3O_4/Ni Foam. (e) X-ray energy spectrum analysis of element distribution images of Co_3O_{4-x}@C/Ni Foam. (f) TEM image and high-resolution TEM image (internal image) of the Co_3O_{4-x}@C.

whole collector. Fig. 2f shows a TEM images of single Co_3O_{4-x}@C nanowires containing porous carbon particles. The porous structure can expand the surface area and improve the interaction of electrolyte-electrode interface [53]. The lattice fringes of nanocrystals are further illustrated in high resolution TEM images (Fig. 2f). The crystal plane spacing of 0.47 nm corresponds to the (111) plane of Co_3O_4 crystal.

In order to prove the effect of oxygen vacancy on the valence state of Co, the chemical state of Co on the electrode surface is analyzed by EPR and XPS. EPR results (Figure.S1) showed the generation of vacancies after plasma treatment, which was similar to previous reports [54,55]. Fig. 3 shows the Co 2p electronic region of XPS spectrum. The spectrum mainly contains two peaks, each of which can be fitted with two valence Co peaks. The peaks at 781.3 eV and 796.4 eV are attributed to Co^{2+}, and the peaks at 794.9 eV and 779.7 eV are related to Co^{3+} [56]. Finally, according to the area of the fitting peaks, the ratios of the two valence states of Co_3O_4 after different time argon plasma treatment are calculated respectively. The results are summarized in Table.S1. The ratio of bivalent and trivalent cobalt of Co_3O_4 without argon plasma treatment (Fig. 3a) is 1.00, which is very close to the theoretical value. With the increase of plasma treatment time (1 min, 3 min, 5 min), the proportion of bivalent cobalt increased (55.1%, 58.0%, 61.7%), while the proportion of trivalent cobalt decreased (44.9%, 42.0%, 38.3%), indicating that the oxygen vacancy increases with the increase of plasma treatment time. In order to keep the charge balance of the material, the valence state of transition metal element Co changes. These plasma induced defects can adjust the local electronic environment and surface properties [57,58], and generate more active centers, which makes Co_3O_{4-x} riched in defects have high catalytic performance.

3.2. Electrochemical performance

In order to evaluate the effect of different oxygen vacancies, the untreated catalyst Co_3O_4@C and argon plasma treated materials Co_3O_{4-x}@C (1 min), Co_3O_{4-x}@C (3 min), Co_3O_{4-x}@C (5 min) are measured by rotating disc electrode method (RDE) in 0.1 mol L^{-1} KOH.

The last cycle of CV is taken as the stable result, and the average of the upper and lower curves is taken as the equivalent linear voltammetric sweep curve (LSV). Fig. 4a shows the LSV curves of various catalysts at a scanning rate of 10 mV s^{-1} and a speed of 1600 rpm. Co_3O_{4-x}@C (3 min) shows the most positive onset potential of 0.963 V (vs. RHE), which is 199 mV, 155 mV and 139 mV higher than that of Co_3O_4@C, Co_3O_{4-x}@C (1 min) and Co_3O_{4-x}@C (5 min) which show 0.764 V (vs. RHE), 0.808 V (vs. RHE), 0.808 V (vs. RHE) and 0.824 V (vs. RHE). At the same time, The half wave potential of Co_3O_{4-x}@C (3 min) is 0.671 V (vs. RHE), and the limiting current density of oxygen reduction is 4.84 mA cm^{-2}, which are also significantly higher than those of other catalysts (Table.S2), indicating that moderate oxygen vacancy can significantly improve the catalytic activity of ORR. In terms of the Tafel slope of different materials (Fig. 4b), the Tafel slope decreases significantly after effective plasma treatment. The lowest Tafel slope is 129 mV·dec^{-1} of Co_3O_{4-x}@C (3 min), showing the fastest ORR kinetics [59]. Further RDE measurements to evaluate the polarization curves at different speeds (400–2500 rpm) is shown in Fig. 4c. The Koutecky-Levich (K-L) curve shows linearity at different potentials with the same slope (Fig. 4d). The electron transfer number at 0.50–0.53 V (vs. RHE) is 3.95–4.01, which is clearly proved a fast and effective ORR way of Co_3O_{4-x}@C (3 min) is through the four electron transfer pathway [60]. Moreover, for Co_3O_4@C, Co_3O_{4-x}@C (1 min) and Co_3O_{4-x}@C (5 min) the same tests are done (Figure. S2). At all rotating speeds, there is no plateau in the curve, which clearly

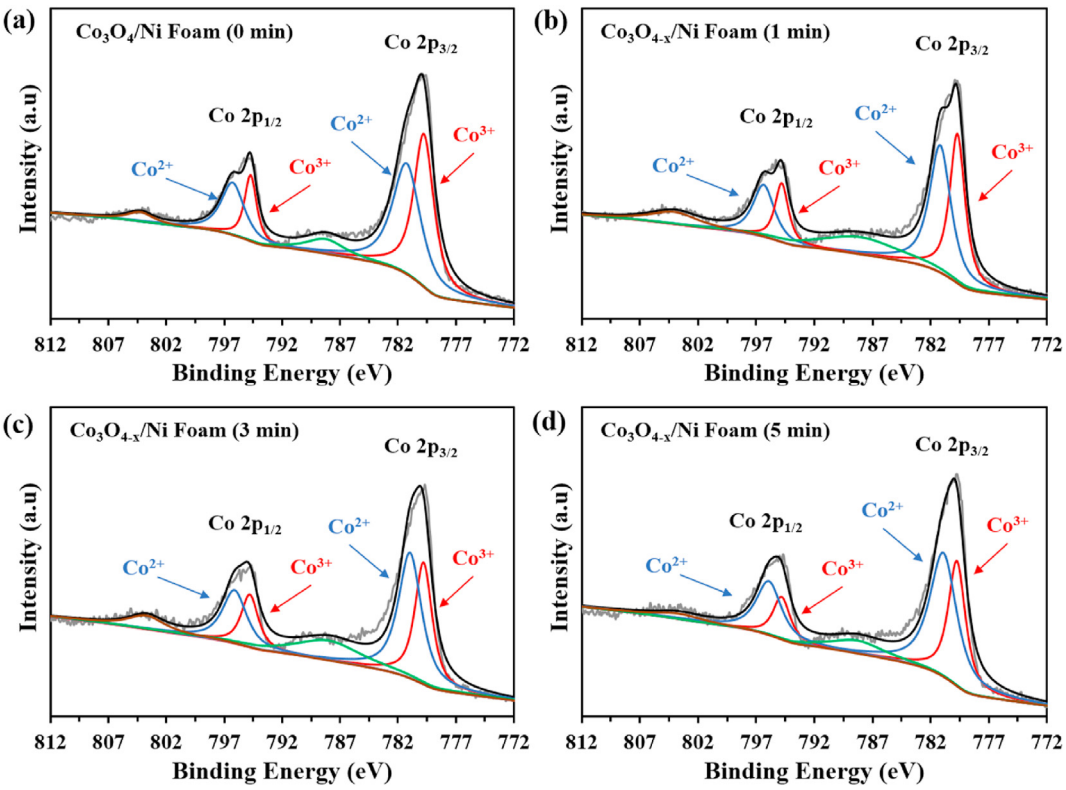

Fig. 3. XPS spectra of materials at different plasma time. (a) Co_3O_4/Ni Foam, (b) Co_3O_{4-x}/Ni Foam (1 min), (c) Co_3O_{4-x}/Ni Foam (3 min), (d) Co_3O_{4-x}/Ni Foam (5 min).

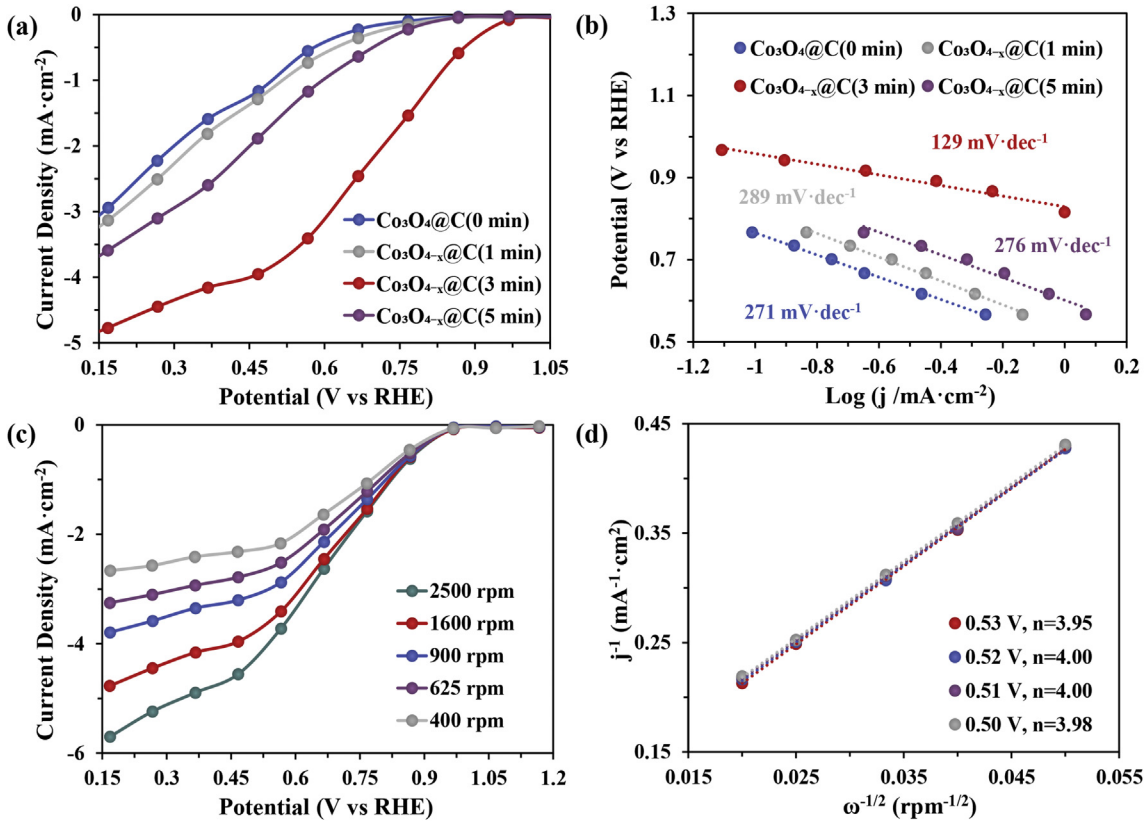

Fig. 4. (a) ORR polarization curves of different electrocatalysts at 1600 rpm speed of RDE and (b) The corresponding ORR Tafel curves. (c) ORR polarization curves of Co_3O_{4-x} (3 min) at different speed of RDE and (d) The corresponding Koutecky–Levich plots at 0.50–0.53 V.

shows that the introduction of oxygen vacancies improves the catalytic activity of Co_3O_4, and the amount of oxygen vacancies needs to be controlled in a moderate range. As a bifunctional electrocatalyst, efficient OER catalytic activity is needed in the process of battery charging. The LSV curves of different catalysts are compared in the voltage range of OER reaction voltage (Figure.S3). The results reveal that the effect of oxygen vacancies on OER activity is not obvious, and Co_3O_{4-x}@C (3 min) shows a small advantage of OER reaction kinetics.

The characteristics of electrochemical double-layer capacitance (Fig. 5) and AC impedance (Figure.S4) of catalyst materials are also tested and analyzed. Although the surface area measured by the double-layer capacitance (C_{dl}) method is uncertain because it is impossible to distinguish between double-layer charging and the adsorption of charged materials [61,62], it is still a reference surface diagnosis tool [52]. The results by clearly show that the C_{dl} (12.5 mF cm^{-2}) of Co_3O_{4-x}@C (3 min) is much higher than that of Co_3O_4 @C, Co_3O_{4-x}@C (1 min), Co_3O_{4-x}@C (5 min) which are 9.2 mF cm^{-2}, 8.7 mF cm^{-2}, 9.7 mF cm^{-2}, respectively (Fig. 5 and Table.S3). The specific calculation and fitting process is shown in Figure.S5. It is strongly proved that higher density of active sites can be produced in the electrocatalyst, which is very beneficial to improve the electrocatalytic activity. In addition, the EIS reveals Co_3O_{4-x}@C (3 min) has better ion and charge transport ability than other materials.

In general, the effect of Ar plasma treatment on the catalytic activity of OER and ORR is different. Because Co^{3+} and p-type Co^{2+} in cobalt based materials are excellent OER active sites [63] and the difference of catalytic activity between these two active sites is small, the OER catalytic activity of Co_3O_4 is high. The introduction of oxygen vacancies has no significant effect on OER. The intrinsic ORR activity of Co_3O_4 is very poor. A large number of oxygen vacancies expose more active site, and the coated porous carbon materials enhance the conductivity of nanoarrays so that the improvement of ORR kinetics is more significant [64]. However, excessive oxygen vacancies can increase the low valence Co, and the energy consumption from the low valence Co to the active intermediate is higher than that from the high valence state, which increase the required energy consumption [24]. What's more, the structural distortion caused by excessive defects can make the ORR kinetics slow down.

3.3. Performance of zinc air battery

To prove the electrochemical performance of Co_3O_{4-x}@C (3 min) in real environment, a rechargeable zinc-air battery (Fig. 6a) is fabricated and its electrochemical performance was evaluated. Previous reports [65,66] showed the electrochemical performance of zinc air battery in oxygen is higher than that in air. The use of oxygen requires additional auxiliary equipment, which will bring additional power consumption and cost to the battery system. Therefore, the results of zinc air battery in the atmosphere were presented to demonstrate the electrochemical performance of the high efficiency catalyst.

The hydrophobic nickel foam collector with catalyst is treated to make the two surfaces have different hydrophobicity (Figure.S6). One surface has high hydrophobicity, which is used as the air side of the air electrode, and the other high hydrophilic surface is soaked in the electrolyte. The electrolyte inlet and outlet are designed in the battery, and the electrolyte is replaced every 24 h. On the one hand, the bubbles generated in the process of charging can be expelled from the battery to prevent the bubbles from accumulating on the

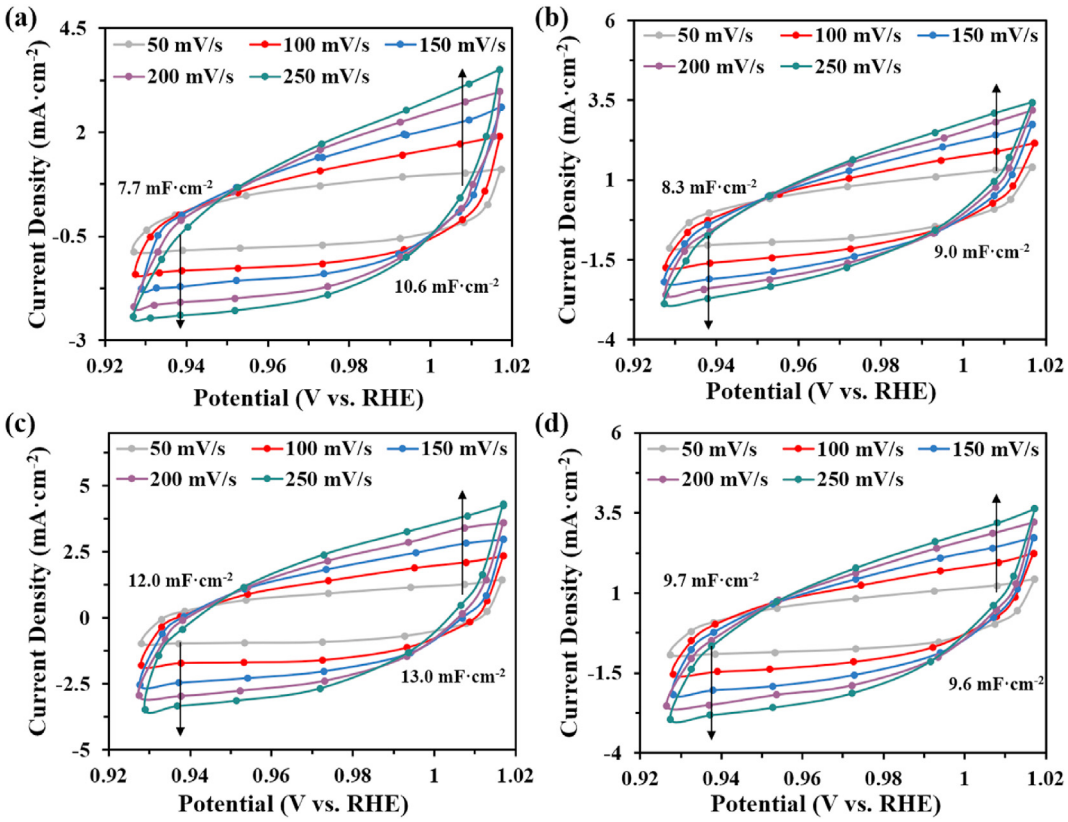

Fig. 5. CV curves and the corresponding specific capacitance of materials at different plasma time. (a) Co_3O_4@C, (b) Co_3O_{4-x}@C (1 min), (c) Co_3O_{4-x}@C (3 min), (d) Co_3O_{4-x}@C (5 min).

surface of the electrode, which can hinder its contact with the electrolyte and reduce the effective reaction area. On the other hand, ZnO deposited in the electrolyte can be filtered out to prevent it from blocking the electrolyte space in the battery.

PTFE is loaded on the Co_3O_{4-x}@C/Ni foam (3 min) and Co_3O_4@C/Ni foam sheets to build the triple-phase boundaries and zinc-air batteries are assembled. Fig. 6b shows the discharge voltage and power density curves. Generally, the open circuit voltage (OCV) of zinc-air battery is about 1.40 V. If the OCV is too high, it may be due to the strong hydrophilicity of air electrode, and the battery system reflects the characteristics of zinc-air/zinc-cobalt oxide hybrid battery. In the actual test, the OCV of the catalyst was 1.38 V, which was slightly higher than the initial value Co_3O_4@C (1.37 V), all of which are typical OCV of zinc-air battery, indicating that the hydrophobic material load of air electrode belongs to moderate range. Due to the poor ORR catalytic activity of Co_3O_4, the discharge performance of the rechargeable zinc-air battery should be evaluated firstly. At the same current density, the discharge voltage plateau of Co_3O_{4-x}@C (3 min) is higher than that of Co_3O_4@C, which brings more power output. For the electrocatalyst Co_3O_{4-x}@C (3 min), a maximum power density of 54.5 mW cm^{-2} is delivered when the current density reaches 83.5 mA cm^{-2}, which is 51.4% higher than that of the electrocatalyst without oxygen vacancies (Co_3O_4@C). It is caused by the improved conductivity and more active sites due to oxygen vacancies.

The stability of zinc-air battery is studied by discharge charging test at the current density of 10 mA cm^{-2}, and the results are shown in Fig. 6c. In the initial 10 cycles for Co_3O_{4-x}@C (3 min), the average voltages of discharge and charge are 1.19 V and 2.06 V, and the charge-discharge voltage gap is 0.87 V. After 360 cycles, the battery continues to work over 180 h. At this time, the average discharge voltage and the average charge voltage is separately 1.13 V and 1.99 V, and the charge-discharge voltage gap is 0.86 V. Comparing to the initial state, the discharge voltage has a downward trend, but the charge-discharge voltage gap do not change significantly. After 700 cycles, the average discharge voltage and the average charge voltage is separately 1.14 V and 1.99 V, and the charge-discharge voltage gap is 0.85 V. During the 700 cycles, there is a downward trend in the discharge curve, but after replacing the electrolyte, the discharge voltage can return to the initial state. It proves that the electrocatalyst Co_3O_{4-x}@C (3 min) shows significant durability so that the charge-discharge voltage gap is kept below 0.90 V. After running for 358 h, the discharge voltage of the zinc-air battery begins to drop rapidly until the battery is completely disabled. The voltage of charge and discharge in different cycling time for both Co_3O_{4-x} (3 min) and Co_3O_{4-x}@C (3 min) are shown in Table.S4. The charge voltage of Co_3O_{4-x}@C (3 min) is slightly higher than that of Co_3O_{4-x} (3 min), which is because the coated carbon keeps active sites away from directly contacting with the electrolyte. It is worth noting that, the discharge voltage of Co_3O_{4-x}@C (3 min) is much higher than that of Co_3O_{4-x} due to a large number of active sites released by oxygen vacancies. Hence, the assembled zinc-air batteries show a completely different trend of charge-discharge voltage gap. For the electrocatalyst without carbon coated Co_3O_{4-x} (3 min), the average charge-discharge voltage gap is 0.84 V at the current density of 10 mA cm^{-2} in the first 10 h. However, due to the lack of protection with carbon layer, the discharge voltage decreases rapidly. The charge-discharge voltage gap increases to 0.97 V after 60 h and 1.08 V after 120 h. It shows that the coated carbon layer is important to improve the cycling stability of oxygen vacancies-rich electrocatalysts, and proves that the optimized catalyst makes Co_3O_4 more suitable for rechargeable zinc-air batteries.

It is worth noting that the curve at the end of the cycle test

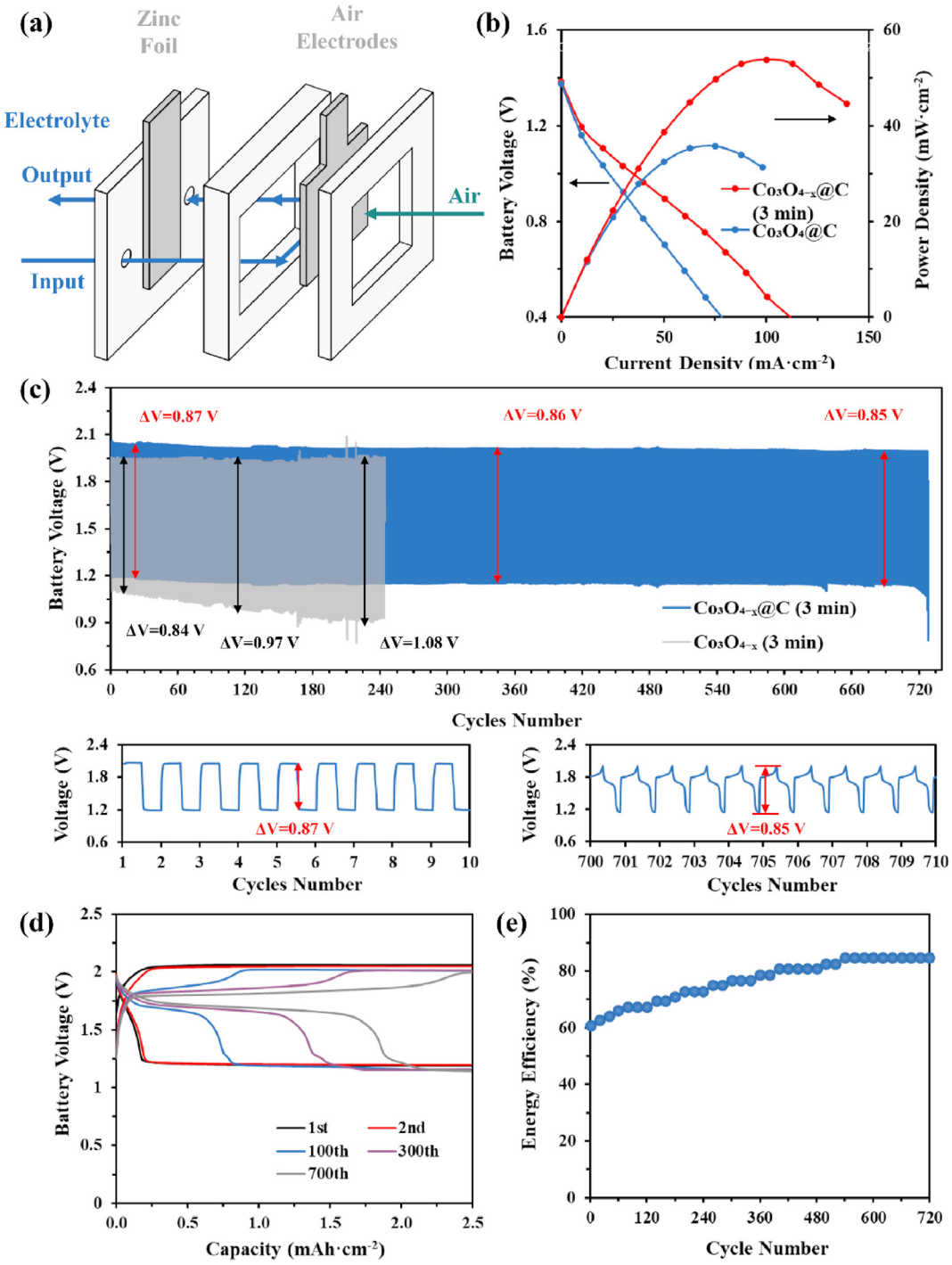

Fig. 6. The electrochemical performance of zinc-air batteries in ambient air. (a) Schematic illustration of rechargeable zinc–air battery. (b) V–I curves and the output power density of zinc-air batteries with Co_3O_4@C/Ni Foam and Co_3O_{4-x}@C/Ni Foam (3 min). (c) Discharge–charge voltage profile of the Zinc–air battery with Co_3O_{4-x}@C/Ni Foam (3 min), the cycle numbers reached 716 cycles (at 10 mA cm^{-2}, 30 min per cycle). (d) Voltage profiles of the 1st, 2nd, 100th, 300th, and 700th cycle. (e) Energy efficiency throughout the cycling test.

reflects the characteristics of zinc-air and zinc-Co_3O_4 hybrid battery [48]. As clearly indicated in Fig. 6d, the flat plateau at the voltage of 1.19 V and 2.02 V are shown in the first charging and discharging process respectively. This represents the typical OER and ORR process of zinc air battery. In the 100th cycle, there are totally four flat voltage plateaus during charging and discharging. This reveals that the evolution and reduction of Co_3O_4 appear in the process of charging and discharging respectively, indicating the gradual formation of hybrid batteries [51]. During 720 cycles, the energy efficiency of the battery is maintained in the high range of 60.7%–84.8%, which is attributed to the hybrid characteristics (Fig. 6e).

After the cycle test, the mass of air electrode is measured and found no obvious change. Moreover, when compared with the catalyst Co_3O_{4-x} (3 min) without carbon coating treatment, it is found that the charge-discharge cycle time of Co_3O_{4-x} (3 min) is greatly increased, which indicates the high stability of carbon-coated oxygen vacancies-rich crystal structure. The peak power density and charge-discharge cycle life are significantly increased

when compared with the data of the same type catalyst in some reports (Table.S5). Hence, the electrode grown on nickel foam with carbon-coated oxygen vacancies-rich Co_3O_4 nanoarrays is a promising air electrode for high performance rechargeable zinc-air batteries.

4. Conclusions

In this work, we used hydrothermal, argon plasma and immersion calcination methods to grow carbon-coated oxygen vacancies-rich Co_3O_4 nanoarrays on the nickel foam. SEM and TEM analysis showed that the plasma treatment introduced a large number of oxygen vacancies on the surface of Co_3O_4 nanoarrays, which endowed more active centers, and improved the performance of oxygen reduction reaction. The concentration of oxygen vacancies and edge can be controlled by the plasma treatment time, and the balance between the density of active centers and the energy consumption can be achieved with a moderate amount of vacancies, which can maximize the catalytic activity. The results show that the open circuit voltage of rechargeable zinc-air battery was 1.38 V and the peak power density is 54.5 mW cm^{-2}. Due to the conductivity and structural protection of carbon coating, the zinc-air battery can be charged and discharged continuously for 716 cycles (358 h) at a current density of 10 mA cm^{-2}, which significantly broaden the cycle life. This discovery will help to expand the application range of cheap Co_3O_4 catalyst and provide an effective and economic way to obtain excellent electrocatalysts for metal-air batteries.

Credit author statement

Dongfang Chen: Conceptualization, Methodology, Writing – original draft. Lyuming Pan: Conceptualization, Data curation, Writing – review & editing. Pucheng Pei: Supervision. Shangwei Huang: Software, Investigation. Peng Ren: Investigation. Xin Song: Visualization.

Declaration of competing interest

The authors declare that they have no known competing financial interests or personal relationships that could have appeared to influence the work reported in this paper.

Acknowledgments

This work is funded by the National Key Research and Development Program of China (Nos.2017YFB0102705 and 2016YFB0101305) and National Natural Science Foundation of China (Nos.21975143 and 21676158).

Appendix A. Supplementary data

Supplementary data to this article can be found online at https://doi.org/10.1016/j.energy.2021.120142.

References

[1] Chu S, Majumdar A. Opportunities and challenges for a sustainable energy future. Nature 2012;488(7411):294–303.
[2] Armand M, Tarascon JM. Building better batteries. Nature 2008;451(7179):652–7.
[3] Pei PC, Zhou QB, Wu L, Wu ZY, Hua JF, Fan HM. Capacity estimation for lithium-ion battery using experimental feature interval approach. Energy 2020;203:6.
[4] Shen D, Wu L, Kang G, Guan Y, Peng Z. A novel online method for predicting the remaining useful life of lithium-ion batteries considering random variable discharge current. Energy 2021:218.
[5] Xu T, Peng Z, Wu L. A novel data-driven method for predicting the circulating capacity of lithium-ion battery under random variable current. Energy 2021:218.
[6] Iranzo A, Arredondo CH, Kannan AM, Rosa F. Biomimetic flow fields for proton exchange membrane fuel cells: a review of design trends. Energy 2020;190:18.
[7] Lin R, Wang H, Zhu Y. Optimizing the structural design of cathode catalyst layer for PEM fuel cells for improving mass-specific power density. Energy 2021:221.
[8] Ren P, Pei PC, Li YH, Wu ZY, Chen DF, Huang SW. Degradation mechanisms of proton exchange membrane fuel cell under typical automotive operating conditions. Prog Energy Combust Sci 2020;80:44.
[9] Meng L, Zhang Y, Wan X, Li C, Zhang X, Wang Y, et al. Organic and solution-processed tandem solar cells with 17.3% efficiency. Science 2018;361(6407):1094–8.
[10] Kim DI, Lee JW, Jeong RH, Yang JW, Park S, Boo J-H. Optical and water-repellent characteristics of an anti-reflection protection layer for perovskite solar cells fabricated in ambient air. Energy 2020:210.
[11] Cheng J, Hu S-C, Sun G-T, Kang K, Zhu M-Q, Geng Z-C. Comparison of activated carbons prepared by one-step and two-step chemical activation process based on cotton stalk for supercapacitors application. Energy 2021:215.
[12] Zha X, Wu Z, Cheng Z, Yang W, Li J, Chen Y, et al. High performance energy storage electrodes based on 3D Z-CoO/rGO nanostructures for supercapacitor applications. Energy 2021:220.
[13] Liu X, Xue JL. The role of Al2Gd cuboids in the discharge performance and electrochemical behaviors of AZ31-Gd anode for Mg-air batteries. Energy 2019;189:8.
[14] Tang M, Chang JC, Kumar SR, Lue SJ. Glyme-based electrolyte formulation analysis in aprotic lithium-oxygen battery and its cyclic stability. Energy 2019;187:7.
[15] Chen XC, Zhou Z, Karahan HE, Shao Q, Wei L, Chen Y. Recent advances in materials and design of electrochemically rechargeable zinc-air batteries. Small 2018;14(44):29.
[16] Sarma DD, Shukla AK. Building better batteries: a travel back in time. ACS Energy Lett 2018;3(11):2841–5.
[17] Wang KL. Solutions for dendrite growth of electrodeposited zinc. ACS Omega 2020;5(18):10225–7.
[18] Wang KL, Pei PC, Wang YC, Liao C, Wang W, Huang SW. Advanced rechargeable zinc-air battery with parameter optimization. Appl Energy 2018;225:848–56.
[19] Sangeetha T, Chen PT, Yan WM, Huang KD. Enhancement of air-flow management in Zn-air fuel cells by the optimization of air-flow parameters. Energy 2020;197:9.
[20] Huang S, Li H, Pei P, Wang K, Xiao Y, Zhang C, et al. A dendrite-resistant zinc-air battery. iScience 2020;23(6):101169.
[21] Wang KL, Liu XT, Pei PC, Xiao Y, Wang YC. Guiding bubble motion of rechargeable zinc-air battery with electromagnetic force. Chem Eng J 2018;352:182–7.
[22] Han XP, Li XP, White J, Zhong C, Deng YD, Hu WB, et al. Metal-air batteries: from static to flow system. Adv Energy Mater 2018;8(27):28.
[23] Pei PC, Wang KL, Ma Z. Technologies for extending zinc-air battery's cyclelife: a review. Appl Energy 2014;128:315–24.
[24] Cheng FY, Chen J. Metal-air batteries: from oxygen reduction electrochemistry to cathode catalysts. Chem Soc Rev 2012;41(6):2172–92.
[25] Seh ZW, Kibsgaard J, Dickens CF, Chorkendorff IB, Norskov JK, Jaramillo TF. Combining theory and experiment in electrocatalysis: insights into materials design. Science 2017;355(6321):1.
[26] Wang YJ, Long WY, Wang LL, Yuan RS, Ignaszak A, Fang BZ, et al. Unlocking the door to highly active ORR catalysts for PEMFC applications: polyhedron-engineered Pt-based nanocrystals. Energy Environ Sci 2018;11(2):258–75.
[27] Roudbari MN, Ojani R, Raoof JB. Performance improvement of polymer fuel cell by simultaneously inspection of catalyst loading, catalyst content and ionomer using home-made cathodic half-cell and response surface method. Energy 2019;173:151–61.
[28] Beltran-Gastelum M, Salazar-Gastelum MI, Flores-Hernandez JR, Botte GG, Perez-Sicairos S, Romero-Castanon T, et al. Pt-Au nanoparticles on graphene for oxygen reduction reaction: stability and performance on proton exchange membrane fuel cell. Energy 2019;181:1225–34.
[29] Suntivich J, May KJ, Gasteiger HA, Goodenough JB, Shao-Horn Y. A perovskite oxide optimized for oxygen evolution catalysis from molecular orbital principles. Science 2011;334(6061):1383–5.
[30] Bhuvanendran N, Ravichandran S, Jayaseelan SS, Xu Q, Khotseng L, Su H. Improved bi-functional oxygen electrocatalytic performance of Pt-Ir alloy nanoparticles embedded on MWCNT with Pt-enriched surfaces. Energy 2020:211.
[31] Debe MK. Electrocatalyst approaches and challenges for automotive fuel cells. Nature 2012;486(7401):43–51.
[32] Cheng FY, Su Y, Liang J, Tao ZL, Chen J. MnO_2-Based nanostructures as catalysts for electrochemical oxygen reduction in alkaline media. Chem Mater 2010;22(3):898–905.
[33] Lima FHB, Calegaro ML, Ticianelli EA. Electrocatalytic activity of manganese oxides prepared by thermal decomposition for oxygen reduction. Electrochim Acta 2007;52(11):3732–8.
[34] Mao LQ, Zhang D, Sotomura T, Nakatsu K, Koshiba N, Ohsaka T. Mechanistic study of the reduction of oxygen in air electrode with manganese oxides as

electrocatalysts. Electrochim Acta 2003;48(8):1015–21.
[35] Han C, Li WJ, Liu HK, Dou SX, Wang JZ. Design strategies for developing non-precious metal based bi-functional catalysts for alkaline electrolyte based zinc-air batteries. Mater Horiz 2019;6(9):1812–27.
[36] Pan J, Tian XL, Zaman S, Dong ZH, Liu HF, Park HS, et al. Recent progress on transition metal oxides as bifunctional catalysts for lithium- air and zinc- air batteries. Batteries Supercaps 2019;2(4):336–47.
[37] Xiao CX, Luo JJ, Tan MY, Xiao YY, Gao BF, Zheng Y, et al. Co/CoN_x decorated nitrogen-doped porous carbon derived from melamine sponge as highly active oxygen electrocatalysts for zinc-air batteries. J Power Sources 2020;453:10.
[38] Wang X, Zhu ZY, Chai LL, Ding JY, Zhong L, Dong AR, et al. Generally transform 3-dimensional In-based metal-organic frameworks into 2-dimensional Co,N-doped carbon nanosheets for Zn-air battery. J Power Sources 2019;440:9.
[39] Tan P, Chen B, Xu HR, Cai WZ, He W, Ni M. Porous Co_3O_4 nanoplates as the active material for rechargeable Zn-air batteries with high energy efficiency and cycling stability. Energy 2019;166:1241–8.
[40] Wang CC, Hung KY, Ko TE, Hosseini S, Li YY. Carbon-nanotube-grafted and nano-Co_3O_4-doped porous carbon derived from metal-organic framework as an excellent bifunctional catalyst for zinc-air battery. J Power Sources 2020;452:10.
[41] Ugalde AR, Kesler O, Naguib HE. Highly stable bifunctional catalyst for Zn-Air batteries: the effect of a nitrated carbon support on Co_3O_4 activity. J Power Sources 2020;453:12.
[42] Park MG, Lee DU, Seo MH, Cano ZP, Chen ZW. 3D ordered mesoporous bifunctional oxygen catalyst for electrically rechargeable zinc-air batteries. Small 2016;12(20):2707–14.
[43] Du GJ, Liu XG, Zong Y, Hor TSA, Yu AS, Liu ZL. Co_3O_4 nanoparticle-modified MnO_2 nanotube bifunctional oxygen cathode catalysts for rechargeable zinc-air batteries. Nanoscale 2013;5(11):4657–61.
[44] Fu J, Hassan FM, Li JD, Lee DU, Ghannoum AR, Lui G, et al. Flexible rechargeable zinc-air batteries through morphological emulation of human hair array. Adv Mater 2016;28(30):6421–8.
[45] Guan C, Sumboja A, Wu HJ, Ren WN, Liu XM, Zhang H, et al. Hollow Co_3O_4 nanosphere embedded in carbon arrays for stable and flexible solid-state zinc-air batteries. Adv Mater 2017;29(44):9.
[46] Wu MJ, Zhang GX, Wu MH, Prakash J, Sun SH. Rational design of multifunctional air electrodes for rechargeable Zn-Air batteries: recent progress and future perspectives. Energy Storage Mater 2019;21:253–86.
[47] Yu MH, Wang ZK, Hou C, Wang ZL, Liang CL, Zhao CY, et al. Nitrogen-doped Co_3O_4 mesoporous nanowire arrays as an additive-free air-cathode for flexible solid-state zinc-air batteries. Adv Mater 2017;29(15):7.
[48] Ma LT, Chen SM, Pei ZX, Li HF, Wang ZF, Liu ZX, et al. Flexible waterproof rechargeable hybrid zinc batteries initiated by multifunctional oxygen vacancies-rich cobalt oxide. ACS Nano 2018;12(8):8597–605.
[49] Liu ZQ, Cheng H, Li N, Ma TY, Su YZ. $ZnCo_2O_4$ quantum dots anchored on nitrogen-doped carbon nanotubes as reversible oxygen reduction/evolution electrocatalysts. Adv Mater 2016;28(19):3777–84.
[50] Tan P, Chen B, Xu HR, Cai WZ, He W, Ni M. In-situ growth of Co_3O_4 nanowire-assembled clusters on nickel foam for aqueous rechargeable Zn-Co_3O_4 and Zn-air batteries. Appl Catal B Environ 2019;241:104–12.
[51] Tan P, Chen B, Xu HR, Cai WZ, He W, Ni M. Investigation on the electrode design of hybrid Zn-Co_3O_4/air batteries for performance improvements. Electrochim Acta 2018;283:1028–36.
[52] Wei C, Rao RR, Peng JY, Huang BT, Stephens IEL, Risch M, et al. Recommended practices and benchmark activity for hydrogen and oxygen electrocatalysis in water splitting and fuel cells. Adv Mater 2019;31(31):24.
[53] Cheng FY, Chen J. Lithium-air batteries: something from nothing. Nat Chem 2012;4(12):962–3.
[54] Deori K, Deka S. Morphology oriented surfactant dependent CoO and reaction time dependent Co_3O_4 nanocrystals from single synthesis method and their optical and magnetic properties. CrystEngComm 2013;15(42):8465–74.
[55] Xiao ZH, Huang YC, Dong CL, Xie C, Liu ZJ, Du SQ, et al. Operando identification of the dynamic behavior of oxygen vacancy-rich Co_3O_4 for oxygen evolution reaction. J Am Chem Soc 2020;142(28):12087–95.
[56] Sun YN, Liu JW, Song JJ, Huang SS, Yang NT, Zhang J, et al. Exploring the effect of Co_3O_4 nanocatalysts with different dimensional architectures on methane combustion. ChemCatChem 2016;8(3):540–5.
[57] Xu L, Jiang QQ, Xiao ZH, Li XY, Huo J, Wang SY, et al. Plasma-engraved Co_3O_4 nanosheets with oxygen vacancies and high surface area for the oxygen evolution reaction. Angew Chem Int Ed 2016;55(17):5277–81.
[58] Yan DF, Li YX, Huo J, Chen R, Dai LM, Wang SY. Defect chemistry of nonprecious-metal electrocatalysts for oxygen reactions. Adv Mater 2017;29(48):20.
[59] Han XP, He GW, He Y, Zhang JF, Zheng XR, Li LL, et al. Engineering catalytic active sites on cobalt oxide surface for enhanced oxygen electrocatalysis. Adv Energy Mater 2018;8(10):13.
[60] Kuang M, Wang QH, Han P, Zheng GF. Cu, Co-embedded N-enriched mesoporous carbon for efficient oxygen reduction and hydrogen evolution reactions. Adv Energy Mater 2017;7(17):8.
[61] Chen QS, Solla-Gullon J, Sun SG, Feliu JM. The potential of zero total charge of Pt nanoparticles and polycrystalline electrodes with different surface structure the role of anion adsorption in fundamental electrocatalysis. Electrochim Acta 2010;55(27):7982–94.
[62] Yoon Y, Yan B, Surendranath Y. Suppressing ion transfer enables versatile measurements of electrochemical surface area for intrinsic activity comparisons. J Am Chem Soc 2018;140(7):2397–400.
[63] Grimaud A, Carlton CE, Risch M, Hong WT, May KJ, Shao-Horn Y. Oxygen evolution activity and stability of $Ba_6Mn_5O_{16}$, $Sr_4Mn_2CoO_9$, and $Sr_6Co_5O_{15}$: the influence of transition metal coordination. J Phys Chem C 2013;117(49):25926–32.
[64] Jiang M, Fu CP, Yang J, Liu Q, Zhang J, Sun BD. Defect-engineered MnO_2 enhancing oxygen reduction reaction for high performance Al-air batteries. Energy Storage Mater 2019;18:34–42.
[65] Li YG, Gong M, Liang YY, Feng J, Kim JE, Wang HL, et al. Advanced zinc-air batteries based on high-performance hybrid electrocatalysts. Nat Commun 2013;4:7.
[66] Li PC, Hu CC, Lee TC, Chang WS, Wang TH. Synthesis and characterization of carbon black/manganese oxide air cathodes for zinc-air batteries. J Power Sources 2014;269:88–97.